Effects of grain size distribution on the permeability of compacting aggregates: results from rock-analogue experiments and microphysical models

André Niemeijer[1,2,3], Derek Elsworth[1,3] and Chris Marone[2,3]*

[1]Department of Energy and Mineral Engineering, The Pennsylvania State University, USA
[2]Department of Geosciences, The Pennsylvania State University, USA
[3]G3 Center and Energy Institute, The Pennsylvania State University, USA

***** *a.r.niemeijer@uu.nl*

ABSTRACT: We investigate the evolution of permeability with porosity and grain size in compacting aggregates of brine-saturated salt. The porosity of aggregates with different initial grain size distributions was reduced by a step-wise application of compactive strain, retaining the effective normal stress <5 MPa. Permeability was measured under measured steady state flow with a pore pressure differential of 0.1 MPa across two granular layers in parallel. We found that permeability decreased with decreasing porosity according to a power law relation, consistent with predictions from capillary models (i.e. Kozeny-Carman Equation), but with an exponent that changes with porosity. The Kozeny-Carman model overestimates observed permeabilities in all experiments by at least one order-of-magnitude as a result of the assumed monodispersed distribution of grain diameters and therefore pore throat sizes. We extend the Kozeny-Carman model using an expression for the tortuosity that is dependent on the actual grain size. The broader grain size distributions, with abundant small grains, returns lower permeabilities than those predicted using the average or median grain size.

1. Introduction

Previous work has shown that permeability is strongly related to the porosity and grain size of rock or fault gouge (Bernabé 1995; Bernabé et al. 2003; Zhang et al. 1994a,b; David et al. 1994; Fredrich et al. 2006; Giger et al. 2007). For most materials, it has been shown that permeability varies with porosity with a power law dependence, ϕ^{α}, where α can take values ranging from 21 to 2 (David et al. 1994b; Zhu, et al.1995; Bernabé et al. 2003), depending on the mechanism of porosity-reduction or creation. Bernabé et al (2003) showed that the value of the apparent power exponent α depends significantly on the deformation mechanism that is operating under the experimental conditions. This is most likely the result of changes in effective pathways through the pore or fracture network that are not directly related to changes in the actual porosity. In order to distinguish between these, Bernabé et al (2003) considered the difference between effective porosity and non-effective porosity. Here, effective porosity is defined as porosity that contributes to (i.e. is part of) the effective fluid flow path and non-effective porosity is any part of the void space within a solid. The non-effective porosity can be pore walls, dead-end pores, sealed cracks or otherwise isolated voids. Changes in non-effective porosity will not lead to changes in permeability and therefore should reduce the sensitivity of the porosity dependence of permeability (i.e. α). However, if the effective porosity consists of an array of different-sized pores in series, the permeability will be mostly controlled by the size of the smallest pore. In such a case, a change in porosity that affects all pores equally should lower the permeability more than for an array of single-sized pores. Clearly, the permeability of a rock with varying grain size distributions, and subject to different deformation mechanisms, will change differently with changing porosity.

Here, we present results from an experimental study on powdered samples of rock salt. This study focuses on the effect of time-dependent compaction by pressure solution on the permeability of granular aggregates to assess the effects of initial grain size distribution on the porosity-permeability relation.

2. Background

One of the most widely used models defining permeability of granular aggregates as a function of grain size and porosity, is the Kozeny-Carman (KC) equation (Kozeny 1927; Carman 1937). The KC-model is based on the Poiseuille Equation for the average velocity of an incompressible uniform liquid (Newtonian liquid) in a cylindrical tube of constant radius R:

$$V_{ave} = \frac{1}{8\mu} R^2 \frac{dP}{dx} \tag{1}$$

where V_{ave} is the average flow velocity (m/s), μ is the viscosity of the liquid and dP/dx is the pressure gradient. In order to account for the variation in the size of the flow channels in a natural sample, a characteristic dimension is needed to describe the average size of the flow channel. The hydraulic radius (R_H=cross sectional area of the flow channel/wetted perimeter) is often used and Equation (1) in terms of flow rate becomes:

$$q = C_s \frac{1}{\mu} R_H^2 A_{flow} \frac{dP}{dx} \tag{2}$$

where C_s is a shape factor for the cross section of the tube (1/2 for a circle) and A_{flow} is the cross-sectional area of the tube. Now, for a bundle of fully saturated parallel capillaries of constant but irregular cross section, contributing to a total cross section (see Figure 1), the area of flow passages is given by

$$A_{flow} = \varphi A_{total} \tag{3}$$

The hydraulic radius is given by

$$R_H = \frac{A_{flow}}{P} = \frac{A_{flow} L}{PL} = \frac{V_{water}}{S_0} \tag{4}$$

where P is the wetted perimeter, L is the length of the flow channel in the direction of flow and S_0 is the specific surface area per unit volume of particles. Assuming full saturation of the aggregate, the volume of water is given by

$$V_{water} = \varphi \cdot V_s \tag{5}$$

Combining equations (3), (4) and (5) into (2) gives:

$$q = C_s \frac{1}{\mu} \left(\frac{\varphi \cdot V_s}{S_0}\right)^2 \varphi \cdot A_{total} \frac{dP}{dx} = C_s \frac{1}{\mu} \frac{V_s^2}{S_0^2} \varphi^3 A_{total} \frac{dP}{dx} \tag{6}$$

Now, by analogy with Darcy's law, the hydraulic conductivity is:

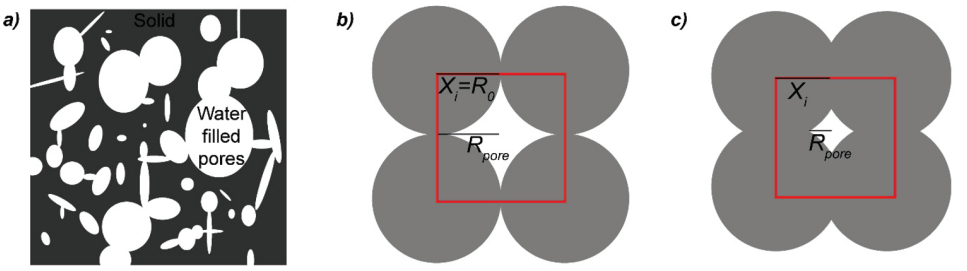

Figure 1: a) Schematic representation of variably shaped pores in natural samples b) Idealized geometry (Simple Cubic packing) at maximum porosity allowing the calculation of the pore radius and area (see e.g. Pluymakers & Spiers 2014) c) the grain aggregate of b) at an arbitrary lower porosity.

$$K_h = C_s \frac{1}{\mu} \frac{V_s^2}{S_0^2} \varphi^3 \tag{7}$$

and the permeability is given by:

$$k = K_h \mu = C_s \frac{V_s^2}{S_0^2} \varphi^3 \tag{8}$$

which is one form of the Kozeny-Carman Equation. Now, C_s can be expressed as a function of the pore shape and tortuosity (effective path length):

$$C_s = \frac{1}{k_0 T^2} \tag{9}$$

where k_0 is a pore shape factor (usually taken as 2.5) and T is the tortuosity (usually taken as $\sqrt{2}$).

In this formulation, the grain size dependence of permeability is expressed through the definition of the hydraulic radius, which can be readily adjusted to fit the experimental data. Moreover, the KC model has so far been mostly applied using a single magnitude for the hydraulic radius and by extension the grain size, whereas natural samples always show a grain size distribution. An aggregate with a distributed grain size will have a lower permeability than an aggregate consisting of single sized grains, as finer grains will occlude the larger pores, thus reducing the effective pore size and increasing the tortuosity. Here, we extend the original KC formulation to accommodate a distributed grain size. To do this, we start again with equation (1), but now using the actual radius of the pore:

$$V_{ave} = \frac{1}{8\mu} R_{pore}^2 \frac{dP}{dx} \tag{10}$$

And the flow rate and permeability will thus be:

$$q = C_s \frac{1}{\mu} R_{pore}^2 A_{pore} \frac{dP}{dx} \tag{11}$$

$$K = C_s R_{pore}^2 \frac{A_{pore}}{A_{total}} \quad (12)$$

where A_{pore} and A_{total} are defined in Figure 1. We use a simple geometrical model of perfect spheres in simple cubic packing, deforming by intergranular penetration as a result of pressure solution, allowing the contact areas to grow and the pore sizes to decrease (see Figure 1 and Pluymakers & Spiers 2015). We further use a random number generator to generate up to 10000 different grain sizes from a desired grain size distribution and calculate the permeability for each grain size according to (9) and (12). The values for the pore area, total area and pore size are calculated for each magnitude of porosity. To accommodate the increase in tortuosity and decrease in pore size for a broader grain size distribution, we define the tortuosity as:

$$T = \frac{c^2}{x_i^2}\sqrt{2} \quad (13)$$

where c is the mean grain size of the distribution and x_i is the current grain size. After calculating the permeability for each individual grain size for a given porosity, the bulk permeability is calculated by taking the geometric mean (equivalent to all pores in parallel) and the harmonic mean (equivalent to all pores in series) of the distribution of permeability values.

3. Experimental methods

A series of stress relaxation experiments were performed on simulated fault gouges consisting of granular rock salt in a double-direct shear configuration with a true triaxial pressure vessel (Samuelson et al. 2009). The rock salt was ground and sieved to obtain initial grain sizes in the ranges 38-106, 53-106 and 63-90 μm (see Table 1). The loading platens (Figure 3a) are plumbed to allow pore fluid access. To ensure an even distribution of the pore fluid pressure over the sample area, porous stone plates or sintered stainless steel plates ("frits") were used. The permeability of the frits was tested using a dummy sample of glass beads (d= 0.5 mm and $k=10^{-8}$ m^2) and was found to be higher than the maximum permeability measurable with the diameter of the tubing used (~$5x10^{-13}$ m^2). Samples were prepared by loading the side blocks with approximately 45 grams of material, yielding two layers with an initial thickness of ~ 6 mm. The loaded side blocks were attached to the center block and the entire sample assembly was placed inside a set of rubber membranes (see Samuelson et al. 2009). The sample was sealed by winding steel wire around the three loading blocks, effectively sealing the rubber membrane against the O-rings. The sealed assembly was then placed inside the pressure vessel which is located inside a biaxial loading frame and the sample was compacted under room-dry conditions for 15 minutes at an applied horizontal stress of 5 MPa.

After the completion of dry compaction, the thickness of the sample assembly was measured on the bench and the assembly was returned to the pressure vessel. A horizontal stress of ~0.5 MPa was applied to keep the assembly in place while connecting the fluid inlet and outlet lines to the vessel fittings. Then, the pressure vessel was closed and filled with the confining fluid (XCELTHERM® 600 oil from Radco Industries). At the same time, the horizontal piston was switched to displacement control mode. The desired confining pressure (2 MPa) was applied using the pressure intensifier and servo-controlled at 2 MPa during the entire experiment (variation < 0.05 MPa). At this point, the "zero" load signal and "zero" horizontal position were recorded. Pore fluid was introduced into the system by attaching pore fluid tube A to the pressure vessel and slowly elevating the pressure in intensifier A, so that the applied pore pressure did not exceed 0.1 MPa. After ~ 30 mm of displacement on pore pressure intensifier A, breakthrough occurred of the pore fluid from outlet B. Next, pore

fluid tube B was attached to the vessel and a pore pressure of 0.1 MPa was applied by pressure intensifier A in servo-controlled mode. The sample was subsequently loaded horizontally at such a rate that the normal stress never exceeded 10 MPa until the desired porosity (i.e. horizontal displacement) was achieved. The sample was allowed to relax to hydrostatic stress and a pressure differential was applied across the sample by lowering pore pressure B (usually to 0.05 MPa, i.e. ΔP=0.05 MPa). The flow rate was measured by the movement of both pore pressure intensifiers. Once steady state flow was achieved (as evidenced by equal flow rates in A and B), the pressure differential was maintained for an additional 15-30 mm of displacement on the pore pressure pistons. Then, the valve on pore pressure intensifier B was closed and the sample was again horizontally loaded and allowed to relax.

In this manner, the permeability of the samples was determined for different porosities in a step-wise fashion. At the end of the experiment, the pore pressure and confining pressure were removed, and the sample assembly was flushed with compressed air. The final thickness of the sample assembly was recorded, and the sample was disassembled. The two compacted layers were carefully removed from the loading blocks and flushed with iso-butanol to remove any remaining brine. The samples were then dried at 50 ºC for 24 hours before impregnation with epoxy and subsequent thin sectioning for SEM and microscope analysis.

Table 1: List of all experiments reported here.[1] Porosity determined from measured layer thickness and weight of salt assuming a density of 2.17 g/cm^3, [2] Final porosities from displacement of horizontal piston,[3] Final porosity determined using Archimedes method. n.d. means not determined.

Experiment	Grain size (µm)	h_0 (mm)	h_{final} (mm)	ϕ_0 [1]	ϕ_{final} [2]	ϕ_{final} [3]
p1327	38-106	10.51	6.66	45.41	16.54	16.9
p1445	38-106	14.06	10.82	36.28	1.72	n.d.
p1490	38-106	15.13	12.29	35.25	8.71	7.2
p1444	53-106	14.04	12.13	32.85	20.19	14.4
p1489	53-106	15.25	12.36	38.33	7.84	11.7
p1498	53-106	14.28	11.93	38.86	11.87	12.0
p1536	53-106	16.95	13.05	40.46	8.12	16.5
p1537	63-90	17.17	13.15	38.48	6.32	12.2

4. 1. Results – Stress relaxation

In Figure 2a, we show the stress relaxation curve for three samples with different initial grain size distributions. In all cases, the applied stress drops rapidly, initially, followed by a more gradual decrease. Stress relaxation rates are highest during the initial part of the experiment (i.e. at high porosities) and for the smallest grain sizes. Moreover, stress relaxes faster for samples with a broader grain size distribution, indicating faster compaction rates for these samples ((Niemeijer et al. 2009). We calculated volumetric strain rates using the elasticity of the samples and the biaxial loading apparatus and show typical results in Figure 2b. The stress dependence of volumetric strain rate is initially high with an exponent of 2 or larger, before decreasing and reaching a value of ~1 in the later stages of the stress relaxation.

4. 2. Results – Permeability

We show the results for flowthrough tests with a constant pore pressure differential in Figure 3a. Upon opening the valve to allow flow, an increase in pore pressure B and a decrease in pore pressure A can be observed, resulting in a lower pressure differential. After an initial transient

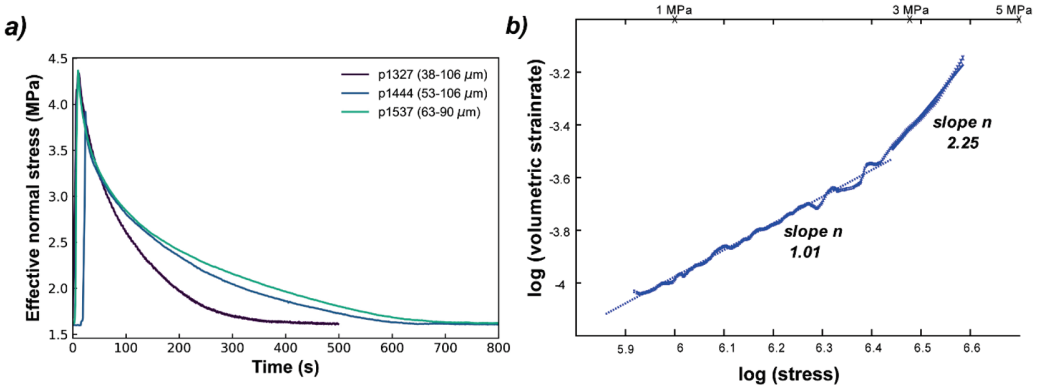

Figure 2 a) Evolution of effective normal stress over time for three experiments with different initial grain size distributions. b) Volumetric strain rate as a function of effective stress during stress relaxation in experiment p1327 (d=38-106 μm, see Table 1).

stage of high flow rates, the flow rate stabilizes, and steady state flow is achieved, which we define as the point at which the flowrates in pistons A & B were within 10% of each other. The duration of the transient stage depended on the storage capacity of the sample and the downstream reservoir and was never longer than ~20 seconds. In calculating flowrates, an averaging window of 5 seconds was used to reduce noise. Permeability was calculated using Darcy' law:

$$k = \frac{Q \cdot l \cdot \mu_f}{A} \Delta P \quad (14)$$

Here, Q is the flow rate through the sample (m^3/s), l is the length of the flow path, in our case the thickness of the sample layers (m), μ_f is the dynamic viscosity of the fluid (N/m^2s), A is the sample area (m^2) and ΔP is the pressure differential (Pa). Permeability decreases with decreasing porosity for all samples (Figure 3b) and this decrease is largest for the samples with the widest grain size distribution.

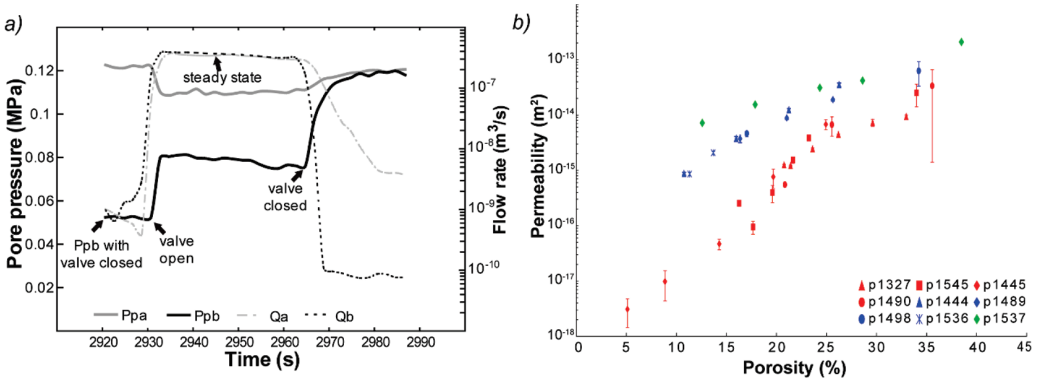

Figure 3: a) Evolution of pore pressure and flowrate as measured in the two fluid intensifiers during a measurement of permeability b) All permeability and porosity data obtained. The grain size fractions used are 38-106 μm (red symbols), 53-106 μm (blue symbols) and 63-90 μm (green symbols).

4.3. Results - Microstructures

In Figure 4a we show a general overview of the microstructure of sample p1327, obtained via X-ray CT scanning using a Zeiss Xradia 610 Versa X-ray microscope. This sample has a final porosity of 16% (see also Table 1), which is also reflected in the microstructure. The final grain size is similar to the initial grain size fractions (38-106 μm) and there is no evidence of intragranular fracturing and grain size reduction. The grain boundaries appear smooth, long and are hard to distinguish. A small number of intact anhydrite grains are randomly distributed throughout the volume. In rare locations, small overgrowths can be observed (Figure 4b).

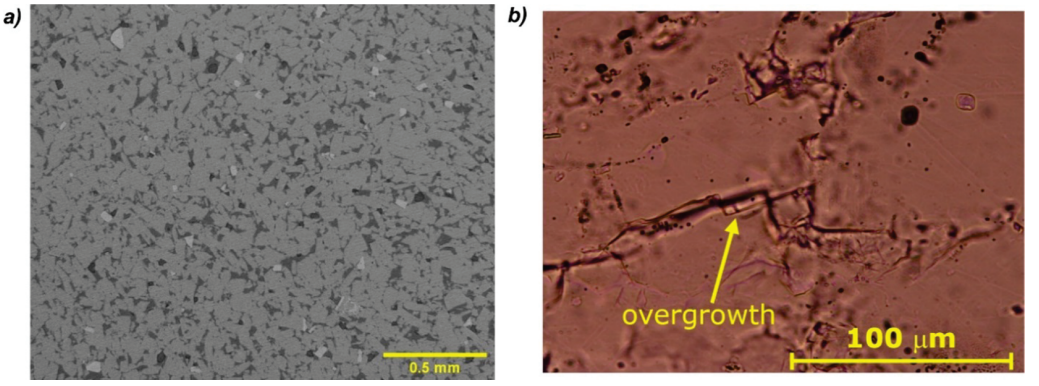

Figure 4: a) X-ray CT image obtained using the Zeiss Xradia 610 microscope of sample p1327. b) Light microscope image of a detail of sample p1327.

5. Discussion

5.1. Deformation mechanism

Under the present experimental conditions, there are a number of possible porosity reducing processes These are 1) cataclasis and associated grain size reduction, grain rotation and rearrangement, 2) dislocation creep and 3) intergranular pressure solution creep. We did not observe significant intragranular fracturing in the final microstructure nor did we observe significant time-dependent porosity reduction during room-dry (~35 % humidity) compaction. Based on these observations, we argue that cataclasis was not a significant porosity reducing process in our samples, although it may play a minor role on the scale of grain contacts.

For pressure solution creep, theory and experiments (Spiers et al. 1989) have demonstrated a stress exponent of 1 for low stress, low strain rate and/or small grain size, whereas the stress

exponent for wet dislocation creep is > 2. The stress exponent we determined is initially >2, indicating some contribution of dislocation creep to the deformation – however, it reduces with ongoing compaction and lower stresses to a value very close to 1. Combining this with the microstructural observations, we conclude that the dominant compaction mechanism was intergranular pressure solution creep with some minor contribution of dislocation creep during initial compaction at high porosity and at correspondingly high stresses at grain-grain contact.

5.2. Effect of porosity and grain distribution on permeability

The data presented in Figure 3b clearly show that permeability of a granular aggregate of salt is dependent on the grain size distribution. Aggregates with a narrow grain size distribution have a permeability that is up to an order of magnitude higher than that of an aggregate with a broad grain size distribution. In Figure 5, we show two realizations of our simple extension to the classical KC model, along with the data of all experiments using a grain size distribution 38-106 μm. For both examples shown, the permeability decreases when a distributed grain size is considered, but it decreases more for a uniform distribution than for a lognormal distribution. This is because the permeability of an aggregate with a lognormal grain size distribution is largely controlled by the most abundant grain size which is the mean grain size. Still, permeability is up to an order of magnitude smaller if we assume that all pores in the distribution are in series (i.e. considering the harmonic mean). Also note that the standard deviation used for this calculation was still relatively small at 15 μm.

In contrast to the KC formulation, our model does not predict a power law dependence of permeability on porosity, i.e.

$$k = k_0 \phi^{\alpha} \quad (15)$$

where α is typically 3. At porosities above 10%, our model predicts a slope significantly above 3 (α=4.27) which seems to better fit the data, especially at porosities above 20%. Results from linear regression of some of the experimental data shown in Figure 5 are listed in Table 2. The loglinear fits are not perfect and there is considerable variability in the slopes for the different experiments. This may reflect uncertainties in the actual porosity values in each experiment, such as those due to small discrepancies in the measured amount of material or in measurements of layer thickness. However, the values of α are consistently larger than 6 and the 95% lower bound value is consistently larger than 3. Spiers and coworkers (1989) reported a value for α of 5.02 for samples with porosity in the range 5-40% and using Argon gas permeametry. They were able to also determine the connected porosity which yielded an exponent of 2.89, much closer to that expected from models based on the hydraulic radius. Unfortunately, we were not able to quantify the connected porosity, but it is likely that our large values for α are similarly caused by the presence of non-effective porosity (Bernabé et al. 2003). As already argued by Bernabé and coworkers (2003), it is the change in effective porosity that will change the permeability. It is the ratio of effective over non-effective porosity (defined as ξ by Bernabé et al. 2003) which controls the magnitude of the power law exponent if we consider total porosity only. Our data and especially the trends in individual experiments suggest that this ratio ξ is not constant during compaction of salt aggregates via pressure solution. Ignoring, for now, data at anomalously low porosities of 5 and 10%, the remainder of the data suggest an increase in the power law exponent α. This is in turn suggests a continuous decrease in the ratio of effective over non-effective porosity ξ, which was also observed by Spiers et al. (1989). Our data are not of sufficiently high quality and density to determine whether there is any change in the manner that the non-effective porosity and thus ξ evolves, although the limited data suggest smaller changes with decreasing porosity for narrower grain size distributions and thus a smaller change in non-effective porosity.

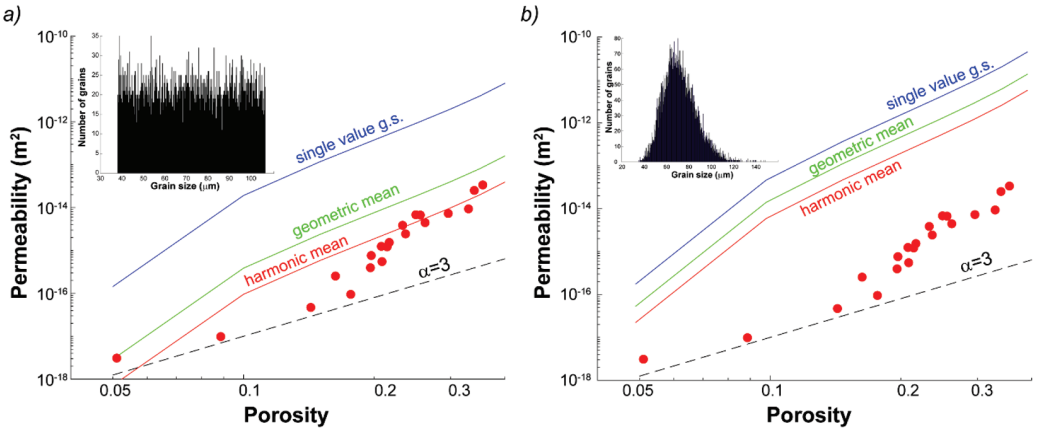

Figure 5: Permeability calculated using Equations 9, 10 and 12, based on SCC packing, evolving through compaction via pressure solution (see Figure 1) for a uniform grain size distribution (a) with minimum and maximum grain sizes of 38 μm and 106 μm, respectively, and a lognormal grain size distribution (b) with a mean grain size of 72 μm and standard deviation of 15 μm. Data points shown are from experiments p1327, p1445, p1490 and p1545.

Table 2: Results of linear regressions on the porosity-permeability data of experiments p1327, p1445, p1490 and p1545 (d=38-106 μm).

Porosity	α	lower 95%	upper 95%	R^2	N	k_0
all	6.27	5.40	7.14	0.93	20	$10^{-10.73}$
> 20%	5.92	4.25	7.60	0.86	13	$10^{-10.88}$
> 10%	6.73	5.46	7.99	0.90	18	$10^{-10.45}$
10-20	5.92	-17.07	28.91	0.38	5	$10^{-10.23}$
20-30	6.95	3.44	10.45	0.76	10	$10^{-11.16}$

6. Summary, limitations, and suggestions for future work

The work presented here demonstrates that it is important to consider the grain size distribution of granular aggregates when modeling the evolution of porosity and permeability with time since permeability at constant porosity is lower in samples with a wider grain size distribution. In fine-grained salt aggregates, compaction *via* pressure solution reduces porosity and permeability rapidly, falling to below 10^{-17} m^2 within a day at room temperature for an average grain size of 72 μm. The relation between permeability and porosity cannot be described by a power law with a single exponent. We posit that this is since not all porosity contributes to the flow network and that the proportion of this non-effective porosity increases with decreasing total porosity. The inability to determine the proportion of non-effective porosity in our sample during the experiments is a severe limitation, which might be solved in future work by employing transient permeametry techniques such as utilizing pressure decay or pressure oscillations. Both methods provide information on the storage capacity of the sample. Ideally, continuous measurements of permeability are desired during ongoing compaction. However, attempts at this resulted in the development of dissolution holes within the sample. Measurements through transient permeametry may prevent the wormholing. Another option is to perform experiments under concurrent X-ray CT, so that the development of porosity may be continuously imaged and quantified.

Acknowledgments

X-ray CT analysis was performed the EPOS-NL MINT facility at Utrecht University with funding from the Dutch Research Council (EPOS-NL.)

References

BERNABÉ, Y. 1995. Pore-scale heterogeneity, energy dissipation and the transport properties of rocks. *Geophysical Research Letters,* 22**,** 1529-1532.

BERNABÉ, Y., U. MOK, & B. EVANS, 2003. Permeability-porosity relationships in rocks subjected to various evolution processes. *Pure and Applied Geophysics,* 160**,** 937-960.

CARMAN, P. 1937. Fluid flow through a granular bed. *Trans. Inst. Chem. Eng.,* 15**,** 150-167.

DAVID, C., WONG, T.-F., ZHU, W. & ZHANG, J. 1994. Laboratory measurement of compaction-induced permeability change in porous rocks: implications for the generation and maintenance of pore pressure excess in the crust. *Pure and Applied Geophysics,* 143**,** 425-455.

FREDRICH, J. T., DIGIOVANNI, A. A. & NOBLE, D. R. 2006. Predicting macroscopic transport properties using microscopic image data. *Journal of Geophysical Research,* 111**.**

GIGER, S. B., TENTHOREY, E., COX, S. F. & FITZ GERARLD, J. D. 2007. Permeability evolution in quartz fault gouges under hydrothermal conditions. *Journal of Geophysical Research,* 112**.**

KOZENY, J. 1927. Uber kapillar Leiting der Wasser in Boden. *Sitzungsber. Akad. Wiss. Wien,* 136**,** 271-306.

NIEMEIJER, A., ELSWORTH, D. & MARONE, C. 2009. Significant effect of grain size distribution on compaction rates in granular aggregates. *Earth and Planetary Science Letters,* 284**,** 386-391.

PLUYMAKERS, A. M. H. & SPIERS, C. J. 2015. Compaction creep of simulated anhydrite fault gouge by pressure solution: theory v. experiments and implications for fault sealing. *Geological Society, London, Special Publications,* 409**,** 107-124.

SAMUELSON, J., ELSWORTH, D. & MARONE, C. 2009. Shear-induced dilatancy of fluid-saturated faults: Experiment and theory. *Journal of Geophysical Research,* 114.

SPIERS, C. J., PEACH, C.J., BRZESOWSKY, R.H., SCHUTJENS, P. M., LIEZENBERG, J. L.& ZWART, H. J. 1989. Long-term rheological and transport properties of dry and wet salt rocks. Luxembourg: Commission of the European Communities.

SPIERS, C. J. & SCHUTJENS, P. M. 1990. Densification of crystalline aggregates by fluid-phase diffusional creep. In *Deformation processes in minerals, ceramics and rocks,* eds. Barber & P. G. Meredith. London.

ZHANG, S., COX, S. F. & PATERSON, M. S. 1994a. The influence of room temperature deformation on porosity and permeability in calcite aggregates. *Journal of Geophysical Research,* 99**,** 15761-15775.

ZHANG, S., PATERSON, M. S. & COX, S. F. 1994b. Porosity and permeability evolution during hot isostatic pressing of calcite aggregates. *Journal of Geophysical Research,* 99**,** 15741-15760.

ZHU, W., DAVID, C. & WONG, T.-F. 1995. Network modeling of permeability evolution during cementation and hot isostatic pressing. *Journal of Geophysical Research,* 100**,** 15451-15464.